Electrochemical properties of oxygen-enriched carbon-based nanomaterials

S.G. Meirinho, A.M. Ferraria, A.M. Botelho do Rego, A.J.S. Fernandes, A.S. Viana, J.C.S. Fernandes, M.C. Oliveira

PII: S1572-6657(20)30647-0

DOI: https://doi.org/10.1016/j.jelechem.2020.114420

Reference: JEAC 114420

To appear in: *Journal of Electroanalytical Chemistry*

Received date: 20 March 2020

Revised date: 18 June 2020

Accepted date: 25 June 2020

Please cite this article as: S.G. Meirinho, A.M. Ferraria, A.M.B. do Rego, et al., Electrochemical properties of oxygen-enriched carbon-based nanomaterials, *Journal of Electroanalytical Chemistry* (2020), https://doi.org/10.1016/j.jelechem.2020.114420

Electrochemical properties of oxygen-enriched carbon-based nanomaterials

S. G. Meirinho[1,#], A. M. Ferraria[3], A. M. Botelho do Rego[3], A. J. S. Fernandes[4], A. S. Viana[5] J.C.S. Fernandes[6], M. C. Oliveira[1*]

[1]*CQ-VR, Dep. Química, Univ. de Trás-os-Montes e Alto Douro, 5000-801 Vila Real, Portugal*

[2]*CQFM and IN and IBB, Instituto Superior Técnico, Univ. de Lisboa, 1049-001 Lisboa, Portugal*

[3]*I3N, Dep. Física., Univ. de Aveiro, Campus de Santiago, 3810-193, Aveiro, Portugal*

[4]*CQB, CQE, Dep. Química e Bioquímica, Fac. de Ciências, Univ. de Lisboa, 1749-016 Lisboa, Portugal*

[5]*CQE, Dep. Engenharia Química, Instituto Superior Técnico, Univ. de Lisboa, 1049-001 Lisboa, Portugal*

[#] *Present address:* Life and Health Sciences Research Institute (ICVS), School of Medicine, University of Minho, Braga, Portugal

* Corresponding author. E-mail: mcris@utad.pt (M. C. Oliveira)

Abstract

The introduction of oxygen moieties on a carbon-based material to enhance the electrode material activity for the oxygen reduction reaction (ORR) is a most unexplored experimental approach due to the risk of reducing the electron-transport ability of the electrode material. Herein, it is shown that carbon nanomaterials generated electrochemically from graphite can simultaneously show an anomalous high content of oxygen functionalities and a high heterogeneous electron transfer rate. This study was demonstrated with a set of four samples, prepared at different galvanostatic conditions. All the samples display a non-ordered carbon network dominated by aromatic rings, a O/C ratio greater than 0.4, but different amounts of various oxygen-containing functionalities. The electron-transport properties of the obtained films were appraised by cyclic voltammetry and electrochemical impedance spectroscopy.

The application of these metal-free electrode materials to the ORR in the alkaline medium has shown a direct correlation between the materials catalytic activity (potential onset, kinetic current and number of electrons transferred) and the ***C***=O amount, whereas a negative correlation was found for ***C***-O. Their excellent ability for the H_2O_2 reduction was also demonstrated. This work opens a new perspective on the use of highly oxidized carbon nanomaterials in electrocatalysis.

Keywords: electrocatalysis, electrochemistry, hydrophilic carbon nanomaterials, electron transfer,

nanostructures.

1. Introduction

180 years have passed since William Groove conceived the first fuel cell. However, the widespread commercial use of this energy converter device is still constrained by the sluggish kinetics of the oxygen reduction reaction (ORR). This explains the significant efforts that have been devoted to finding new ORR catalysts [1,2]. These catalysts can be classified into three categories: noble metal (e.g. Pt and Pd alloys), non-noble metal (e.g. Fe-N-C materials, metal chalcogenides), and metal-free. Special attention has been given to carbon nanomaterials, as metal-free catalysts, due to their long-term stability, good conductivity, easy handling, environmental friendliness and low-cost production [2–4]. However, their electrocatalytic activity and efficiency to convert oxygen in water can be very low, leading mainly to the formation of hydrogen peroxide instead of water, as evidenced by the data attained on traditional carbon electrodes (graphite and glassy carbon), active carbon (Vulcan XC-72) and carbon-based materials derived from biomass sources [5–8]. Several strategies have been proposed to modify the carbon-based material in order to circumvent this constraint. The main approaches rely on the incorporation of a foreign atom on the carbon material, generally called heteroatom-doping. Currently, this designation includes the substitution of sp^2-hybridized carbon atoms in the graphene lattice by the heteroatom and/or the functionalization of carbon-based material by covalently-bonded groups containing the heteroatom. These groups can have electron-donating or electron-withdrawing properties, leading to the breakdown of the charge-neutral sp^2 carbon lattice and formation of charged sites which may facilitate the oxygen adsorption.

Substantial advancements have been achieved by doping the carbon network with nitrogen (by carbon substitution or functionalization), as witnessed by the extensive reviews found in the literature [3,9–11]. But, apart from nitrogen-doping, no significant progress has been attained by doping with other heteroatoms. The introduction of oxygen-containing moieties on the carbon

structure, as an alternative to nitrogen doping, could be a pathway for tailoring the electrocatalytic activity of carbon-based materials towards the oxygen reduction reaction. This strategy was recently applied to carbon fibers [12], carbon nanotubes (CNTs) [13], carbon foams [14] and graphene oxide-CNT hybrid materials [15], where O/C ratio up to 0.1 - 0.2 were achieved. Although it is theoretically predicted that oxygen-containing groups can promote the ORR via a 4-electron pathway [15,16], oxygen-enriched carbon materials are usually not very attractive for the ORR because the incorporation of oxygen in the carbon network is extremely challenging, due to the risk of breaking the conjugated structure, reducing the electron-transport ability.

Encouraged by our recent findings [17,18] that an oxygen-enriched hydrophilic carbon nanomaterial is released from a graphite electrode in the early stages of the anodic polarization, this work aims to investigate the electron-transport ability of high-oxygen content materials generated electrochemically at different stages of the galvanostatic polarization (1, 9 and 18 hours), and their electrocatalytic activity towards the ORR in an alkaline medium. It is important to clarify that although the present study may contribute to the future research of the overall mechanism responsible for the hydrophilic carbon-based material formation, this work is focused in another direction, the exploration of the electrochemical properties of highly oxidized metal-free materials.

The electron-transfer ability of the prepared materials was evaluated by electrochemical impedance spectroscopy (EIS) and cyclic voltammetry (CV) in redox probe solutions and their physical and chemical properties were compared by Raman, X-ray photoelectron spectroscopy (XPS) and atomic force microscopy techniques (AFM).

2. Experimental Section

2.1 Carbon nanomaterials preparation

Carbon nanomaterials were prepared by a galvanostatic polarization using a two-electrode cell with separated compartments containing graphite rods (99.997 %, Goodfellow) as anode and cathode and a phosphate buffer electrolyte (0.030 M, pH = 7.0). Four different sets of nanomaterials were prepared, which differed on the time and/or on the applied current used in the galvanostatic

polarization, Table 1. Keeping the acronym that was previously used to name the hydrophilic carbon nanomaterial that was produced (EHC - Electrogenerated Hydrophilic Carbon) [19], the prepared materials were labeled as EHCz, where z represents the duration of the galvanostatic experiment (e.g. EHC1, for 1-hour electrolysis). To distinguish the EHC material prepared with the same electrolysis duration but different applied currents, a letter was also used (e.g. EHC18a and EHC18b were generated at 0.06 and 0.03 mA cm^{-2}, respectively). Note that EHC9 and EHC18b were electrochemically generated under the same galvanostatic charge (1.94 x 10^3 C). The electrochemical assays were performed under an air atmosphere. The solutions containing the EHC nanomaterials were removed from the anodic compartment and dialyzed with a 3.5-5 kDa molecular weight cut-off membrane. The electrochemical generation of the carbon-based nanomaterials was performed using an Autolab PGSTAT 100 Potentiostat.

EHC	**Experimental Conditions**		
	Current (mA)	**Time (h)**	**Charge (C) x10^3**
EHC1	60	1	0.22
EHC9	60	9	1.94
EHC18a	60	18	3.89
EHC18b	30	18	1.94

Table 1. Galvanostatic conditions for the electrochemical generation of EHC nanomaterials.

2.2 Physicochemical characterization

The carbon content of the EHC solutions was determined by Total Organic Carbon (TOC) analysis using a Formacs HT Skalar carbon analyzer. XPS analysis was performed using an XSAM800 spectrometer from KRATOS. Sample preparation and spectrometer operating conditions were described elsewhere [19]. Spectra were acquired using the software Vision 2 for Windows, Version 2.2.9 (KRATOS). Experimental Binding Energies (BE) were corrected using the charge shifts obtained

from the simultaneous fitting of C 1s regions. This simultaneous fitting was performed with the Solver add-in program of Microsoft Excel. Peak heights, positions, Full Width at Half Maximum (FWHM) and Gaussian-Lorentzian fractions of pseudo-Voigt profiles were fitted. The particular data treatment of C 1s is described below. The sensitivity factors, used for quantification purposes, were the following: 0.318 for C 1s; 0.736 for O 1s; 0.505 for N 1s; 0.964 for Cl 2p; 1.378 for Na 1s, 1.95 for Ca 2p and 0.53 for P 2p. Atomic Force Microscopy (AFM) images were recorded in a Veeco Metrology Multimode 8 HR (Bruker) coupled to Nanoscope V, using Peak Force Tapping (PFT-AFM). The images were acquired at a scan rate of ca. 1.0 Hz, in ambient conditions (ca. 21 ºC), using a ScanAsyst-Air probe (Bruker) with a spring constant of 0.44 N/m. The samples were prepared by placing a drop of solution (~ 20 μL) onto Highly Oriented Pyrolytic Graphite substrates (HOPG), waiting for ca. 2h, rinsing with water and drying with nitrogen.

The micro-Raman analysis was conducted in the backscattering configuration on an HR800 instrument (Horiba Jobin Yvon, Japan), using a 600 lines/mm grating and the 441.6 nm laser line from a HeCd laser (Kimmon IK Series, Japan). Further details were previously described [20]. For this analysis 5 μL of the EHC solution was deposited onto a quartz slide and dried. The procedure was repeated four times, resulting in a total volume of 20 μL. The obtained spectra were treated according with the following steps: 1) background removal based on spectra taken from the substrate region aside from the carbon material; 2) definition of the most relevant contributions to the overall spectrum structure; 3) fitting procedure with the Raman native software (Labspec) using Gauss-Lorentzian functions for each band.

2.3 Electrochemical characterization

The EHC nanomaterials were cast onto a glassy carbon electrode (GCE, 3 mm in diameter). In order to appraise the reproducibility of the electrode preparation, all the electrochemical measurements were carried out with triplicate electrodes. Good reproducibility was found. Prior to the GCE modification, its surface was polished to a mirror finishing using 0.3 μm alumina powder. The electrochemical cell was assembled with the modified glassy carbon working electrode, an Ag/AgCl

(KCl 3 M) reference electrode and a Pt mesh. Deaeration was achieved by bubbling high purity nitrogen through the electrolyte for 20 min. The gas was maintained over the top of the solution during the electrochemical experiments. All the electrochemical measurements were acquired in the Gamry Instruments Interface 1000E Potentiostat equipped with an FRA module, using the Gamry Framework software for data acquisition.

Redox probe concentrations ($Fe(CN)_6^{-3/4-}$ and $Ru(NH_3)_6^{3+}$) were 1.0 mM. The supporting electrolyte was 0.1 M KCl. Comparison of the electron-transfer ability of EHC nanomaterials in $Fe(CN)_6^{-3/4-}$ solution was carried out with two different sets of modified GCE: one containing a carbon loading of 5 μg cm^{-2} (using EHC1 and EHC9) and another containing a carbon loading of 20 μg cm^{-2} (using EHC9, 18a, and 18b). The electron-transfer ability of EHC nanomaterials in $Ru(NH_3)_6^{3+}$ solution was appraised on GCEs cast with 5 μL of the EHC solution.

The electrochemical impedance spectroscopy (EIS*)* was carried out in the $Fe(CN)_6^{-3/4-}$ solution. Impedance spectra were recorded at a fixed potential (formal potential) within a frequency range from 100 kHz to 100 MHz with a perturbation amplitude of 15 mV. The impedance diagrams were interpreted with ZView software (Scribner, Inc.).

For the ORR experiments, a 0.1 M NaOH solution saturated with high purity O_2 was used and a gentle oxygen flow was maintained above the cell solution during the electrochemical measurements. A rotating disk electrode connected to a Pine electrode rotator with a Radiometer speed control unit from Autolab was employed. Preliminary tests were undertaken with different carbon loadings in order to choose the appropriate carbon loading for each EHC material (Fig. S1). The linear sweep voltammetry (LSV) was performed from the open circuit potential (OCP) value to -1.2 V (vs. Ag/AgCl; -0.24 V vs RHE) at the scan rate of 20 mVs^{-1} and the RDE measurements were conducted at rotating speeds ranging from 400 to 2100 rpm with the same scan rate. The LSV curves for ORR were plotted as *j*–E where *j* is the current density normalized to the geometric area of the rotating disk electrode (0.071 cm^2). All potentials are given with respect to the reversible hydrogen reference electrode (RHE). The kinetic limiting current density was determined by applying the Koutecky-Levich (KL) equation

$$1/j = 1/j_K + 1/j_L = 1/ B\omega^{1/2} + 1/j_K \quad (1)$$

where, j_K and j_L are the kinetic limiting current density and diffusion-limiting current density, respectively, ω is the angular velocity and B is the Levich constant ($B = 0.62nC_{O2}F\upsilon^{-1/6}D_{O2}^{2/3}$). Herein, n is the number of electrons involved in the ORR and F is the Faraday constant (96485 C mol^{-1}), C_{O2} and D_{O2} are the concentration and the diffusion coefficient of O_2 (1.2 x 10^{-6} mol cm^{-3} and 1.9 x 10^{-5} cm^2 s^{-1}, respectively), and υ is the kinematic viscosity of the electrolyte (0.01 cm^2 s^{-1}) [21]. Despite limitations of KL equation to extract electrokinetic and mechanistic information have been pointed recently [22,23], it provides the first approach to assess the relative catalytic activity of different carbon-based catalysts.

The electrochemical reduction of H_2O_2 was carried out in an O_2-free solution containing 0.85 mM H_2O_2, in 0.1 M NaOH solution. The LSV and CV were recorded on an Autolab PGSTAT 100 Potentiostat. All the electrochemical measurements were carried at room temperature (≅ 23 ºC).

3. Results and Discussion

3.1 Physicochemical characterization

During the galvanostatic polarization of graphite electrodes the colorless solution becomes progressively grey in the anodic compartment. From approximately 9 hours of electrode polarization, a sludge-like residue at the bottom of the anodic compartment is detected. When the EHC sample is removed from the cell this residue is discarded, and only the supernatant solution containing the highly hydrophilic material is used and submitted to dialysis. Dialysed solutions are extremely stable, as no deposit is observed over several months. The carbon content of EHC1, EHC9, EHC18a, and EHC18b solutions (not dialysed) was found to be 18, 267, 63 and 176 mg/L, respectively. The significant decrease observed upon 18 h of electrode polarization is a consequence of the sludge-like residue formation (and rejection). It is suggestive of the aggregation of the hydrophilic nanomaterial when it is submitted to a long electrode polarization essay. This data also

suggests the less efficiency of the electrochemical generation of hydrophilic carbon material at an applied current of 0.03 A compared to 0.06 A, even under the same anodic charge.

The AFM images of the EHC solutions cast on HOPG substrates (Fig. 1) show that EHC nanomaterials generated by long electrode polarization form an irregular surface with a porous and nanogranular structure. This result contrasts with the topographic morphology found on EHC1, where the building blocks seem to aggregate in a 2D nanostructure layer formed by rounded grains with similar size. Accordingly, the surface roughness, illustrated by Rq (Root Mean Square roughness) values is approximately ten times higher on EHC9 and EHC18b, than on EHC1. Further insight into the nanogranular material was obtained by diluting the EHC18b solution with water. It was found that the nanogranular material is formed by agglomerates dispersed over the substrate, with 2 to 10 nm in height.

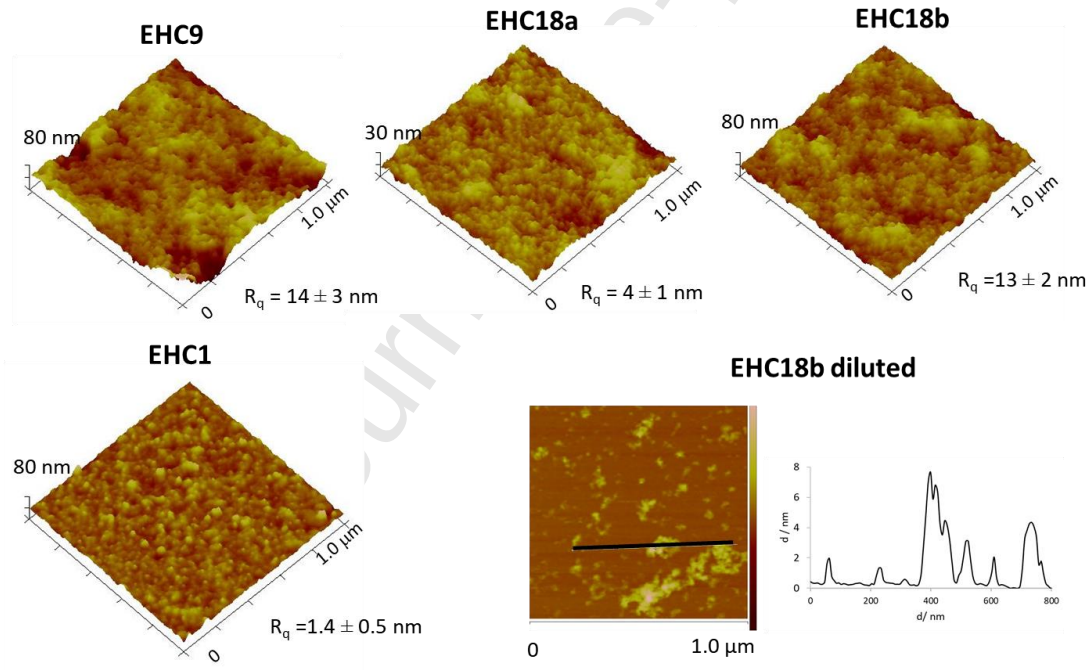

Fig. 1. – 3D AFM images of the different EHC nanomaterials. The bottom right-hand figure includes the 2D AFM image and the height profile of a diluted sample (EHC18b).

The Raman spectra of the four EHC samples (Fig. 2) show the characteristic D band at ≅1360 cm^{-1} and G band at ≅1590 cm^{-1}, typical of carbon sp^2 hybridization. The D band is attributed to the radial breathing modes of 6-fold aromatic rings which only become active in the presence of structural

defects whereas the G band is assigned to the first-order scattering of the E_{2g} vibration mode from the sp^2 carbon domains. For a good fitting of the spectra in the first-order region (≈ 1100 - 1700 cm^{-1}), two other bands were considered. One of them, the D' band, appears as the right shoulder of the G band and is a disorder-induced feature. The other one, centered at ≅ 1540 cm^{-1} (called a-C band) was already mentioned in previously published studies on EHC nanomaterials [20], having been associated with amorphous carbon [24,25].

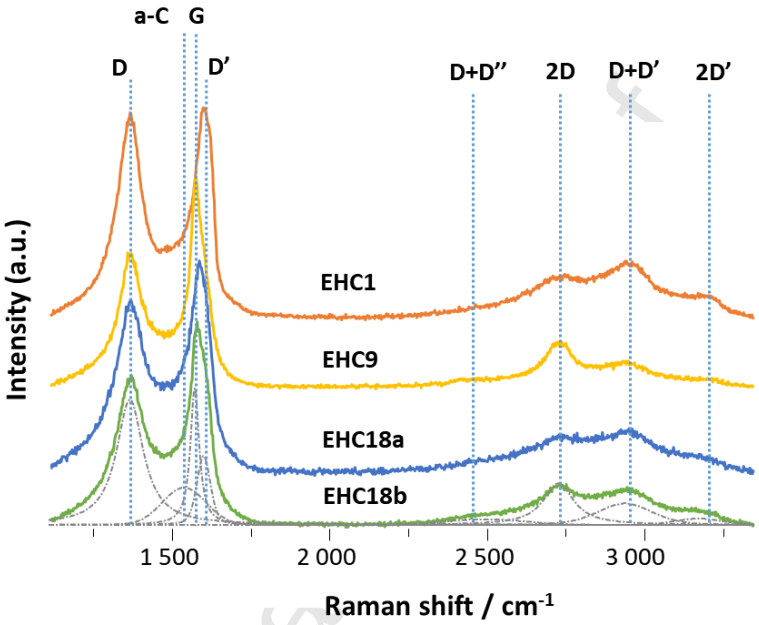

Fig. 2 - Raman spectra of the EHC nanomaterials and the corresponding bands.

The intensity ratios ($I_{a\text{-}C}/I_G$) point for a similar contribution from 1540 cm^{-1} band on both EHC1 and EHC9 materials, as well as on both EHC18a and EHC18b, Table 2. In general, these results reveal that very long electrode polarization periods (18 hours) generate EHC materials with a much higher amorphous degree than shorter polarization stages. However, the second-order region (≈ 2300 - 3300 cm^{-1}) also holds important information. Although some contributions are indistinctive in this region (ex.: D + D'', where D'' appears at ≈ 1150 cm^{-1} from a double resonance process), it is noticeable that the 2D band contribution at ≅ 2740 cm^{-1} (overtone of the D band) is more pronounced in EHC9 and EHC18b than in the other samples, disclosing a higher-order degree. Amorphous carbon does not clearly exhibit this feature, while it is prominent in highly ordered graphite and graphene. All considered this might mean that EHC9 and EHC18b are composed of

amorphous carbon-based material and traces of a higher crystalline degree material. This hypothesis is particularly evident in EHC9, where I_d/I_g ratio is minimum, revealing a lesser defective structure.

EHC	D Peak			G Peak			a-C Peak			I_D/I_G	I_{a-C}/I_G
	Peak Position (cm^{-1})	Intensity (a.u.)	FWHM (cm^{-1})	Peak Position (cm^{-1})	Intensity (a.u.)	FWHM (cm^{-1})	Peak Position (cm^{-1})	Intensity (a.u.)	FWHM (cm^{-1})		
EHC1	1364	597	101	1594	471	48	1542	147	136	1.27	0.31
EHC9	1367	1145	103	1573	1258	34	1539	339	163	0.91	0.27
EHC18a	1366	1479	128	1590	1172	55	1552	685	166	1.26	0.58
EHC18b	1367	1281	124	1573	906	35	1554	562	164	1.41	0.62

Table 2. Peaks position, intensity and FWHM of D-, G- and a-C bands, as well as the I_D/I_G and I_{a-C}/I_G ratio.

The different carbonaceous species existing in the EHC nanomaterials were also studied by XPS. Fig. 3 shows the XPS C 1s regions of all the samples fitted simultaneously with six peaks in the same positions for the different samples having, in each region, equal FWHM and equal Gaussian/Lorentzian %. No constraints were imposed on peak areas. The simultaneous fitting performed with the Microsoft Excel Solver tool led to peaks centred at 285.0 ± 0.1 eV, 286.1 ± 0.1 eV, 287.1 ± 0.1 eV, 288.4 ± 0.1 eV, 289.4 ± 0.1 eV and 290.9 ± 0.1 eV. The fractions and assignments of each peak are shown in Table 3.

The peak at 285 eV can include not only ***C***-H and ***C***-***C*** aliphatic carbon atoms, but also aromatic carbons in agreement with Raman results, which are typical, 0.3 eV to 0.6 eV below the 285 eV peak. The peak centered at 290.9 eV is typical of organic carbonate groups (-O-(***C***O)-O-), although around

this BE one can also find the energy loss region of π-π* electronic excitations in aromatic systems.

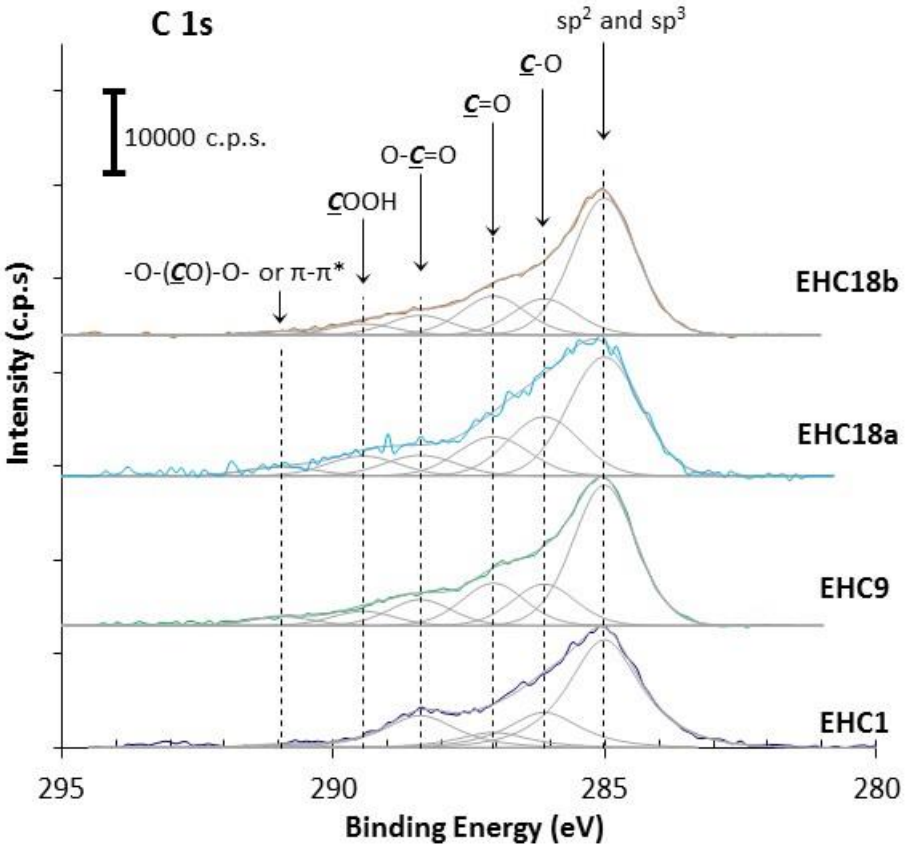

Fig. 3 - C 1s XPS regions. Dashed lines are the positions of the fitted peaks. For detailed assignment see text. The carbon atoms of interest for each BE are highlighted in **bold**, *italic* and underlined. C1s regions are shifted on y-axis for clarity sake.

Actually, all the peaks characteristic of oxidized carbons are at a BE that correspond to functional groups included or nearby aromatic carbon structures: for example, carbon atoms singly-bound to oxygen (***C***-O) like in an ether group (C-O-C) or an alcohol (C-OH) in an aliphatic neighborhood is centered at ~286.7 eV, but in the vicinity of benzene rings it shifts to lower BE (detected at 286.1 eV); the same for the peak centered at 287.1 eV, assigned to carbon doubly bound to oxygen (***C***=O), like in a carbonyl group binding two aromatic rings; the peak fitted at 288.4 eV is most probably from an ester group (O-(***C***O)-) bound to an aromatic chain; the peak at 289.4 eV is typical of

carboxylic groups (-***C***OOH). Table 3 includes all the carbonaceous species found at these BE [26] and the atomic ratio O/C computed through the O 1s and C 1s peak areas. It is shown that EHC materials display indeed an anomalous high O/C ratio, much higher than the commonly oxygen-enriched carbon materials [13,27]. Likely representations of aromatic structures that fit such a high O/C ratio must require the absence of aromatic hydrogen, which has been confirmed by RMN. It is underway advanced spectroscopic characterization of these materials and computational simulation approaches to better elucidate their structure.

	BE (eV)	Atomic Concentrations (%)				Assignments
		EHC1	EHC9	EHC18a	EHC18b	
C 1s	285.0 ± 0.1	55.7	51.1	44.7	55.5	***C***-H, ***C***-***C*** sp^2 and sp^3
	286.1 ± 0.1	18.2	15.2	22.2	14.7	***C***-O-X (X: C, C=O, H) ***C***-N (N is detected in very low relative amounts)
	287.1 ± 0.1	7.9	15.5	14.7	15.8	***C***=O and/or ***C***-***C*** (epoxy)
	288.4 ± 0.1	16.6	9.5	7.7	8.0	XO-***C***=O (X: C or H)
	289.4 ± 0.1	0.0	5.3	7.4	4.5	-***C***OOH and/or ***C***O_3^{2-}
	290.9 ± 0.1	1.6	3.4	3.3	1.5	-O-(***C***O)-O- and/or π-π*
O/C		0.42 ± 0.04	0.45 ± 0.05	0.59 ± 0.06	0.42 ± 0.04	
$O(C_{ox})/C$		0.30-0.61	0.35-0.69	0.41-0.78	0.32-0.62	See Supporting Information for details

Table 3 – Carbonaceous species: fractions of C 1s fitted peaks (at% /(C_{TOTAL} at%) × 100) and assignments; Atomic ratios: $O(C_{OX})/C$ computed from peaks fitted in C 1s assuming minimum and maximum O/C stoichiometries; O/C computed from O 1s and C 1s total areas.

Since the O 1s peak may also include the contribution from inorganic compounds (see Table S1-S3), which may lead to an overestimated O/C ratio, the ratio oxygen/carbon was also estimated taking into account the areas of the peaks fitted to the C 1s region ($O(C_{ox})/C$), Table 3. The range of values

obtained confirms that the anomalous high ratios of O/C are actually due to a significant content of oxygen-carbon containing functionalities. Moreover, it confirms that O/C ratio tends to increase with the duration of the galvanostatic polarization. Quantification of the oxygen-containing functionalities shows how these evolve during the 18 hours of the electrode polarization, Fig.4. The oxygen-containing groups are predominantly in the form of hydroxyl (or ether) and carboxyl on the short-termed electrogenerated materials, and in the form of hydroxyl and carbonyl (or epoxy) on those generated by a long-termed polarization. At this point, we do not have a clear explanation for this carbonaceous profile. It is important to remark that EHC samples generated under the same anodic charge (EHC9 and EHC18b) possess approximately the same carbonaceous composition.

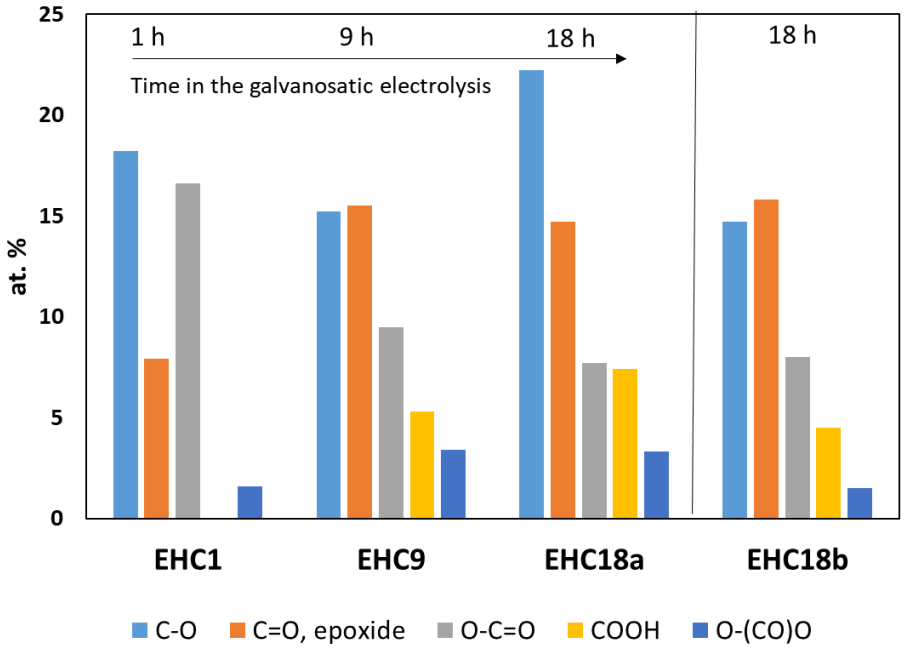

Fig. 4 – Quantification of the oxygen-functionalities on the EHC samples prepared at a different time (EHC 1, EHC9, EHC18a) and at different applied current in the galvanostatic electrolysis (EHC18b).

3.2 Electron-transfer properties

The heterogeneous electron transfer ability of EHC materials was first assessed by cyclic voltammetry in a solution containing ruthenium (III) hexamine. This redox probe is recognized as an exemplar outer-sphere redox couple, insensitive to surface functional group chemistry, but sensitive to the electronic properties of the electrode material.

Fig. 5a and 5b show the voltammograms of 0.1 M $Ru(NH_3)_6^{3+}$ solution at two different scan rates, 20 and 100 mV s^{-1}, respectively. Unexpectedly, the voltammograms recorded on EHC9, EHC18a, and EHC18b materials present a second couple of peaks (A and A´), in addition to the traditional single couple (B and B´). It is important to highlight that no peaks were detected in a $Ru(NH_3)_6^{3+}$ free solution, which means that none of these peaks can be ascribed to functional groups of the carbon material (Fig. S2). At 20 mV s^{-1}, the rather small value of A/A´ peak-to-peak potential separation (ΔEp=16 mV) and the current dependence on the scan rate (Fig. 5c) points out for the adsorption of the positively charged redox probe on the EHC surface. However, the enhancement of ΔEp with the scan rate (ΔEp of 22, 44 and 82 mV at 50, 100 and 200 mV s^{-1}, respectively), strongly indicates that diffusion of the ruthenium hexamine is limited on the timescale of the voltammetric experiments. This behavior is typical of the mass transport regime found on thin-layer cells and on electrodes with a porous layer [28–30]. Accordingly, we ascribe peaks A/A´ to the ruthenium hexamine species that are trapped within the pores of the EHC layer, being unable to react under semi-infinite diffusion conditions as it would be expected for a flat electrode. These results support the different surface morphologies revealed by AFM, pointing out the higher porosity of EHC9 and EHC18b electrode materials, followed by EHC18a and finally by EHC1. In contrast, peaks B/B´are attributed to a reversible one-electron redox reaction under semi-infinite diffusion conditions, as evidenced by the peak-to-peak separation depicted for B/B´ (70-76 mV) and the linear dependence of the current intensity with the square root of the scan rate (only discernible for EHC1 and EHC18a), Fig. 5d.

Although possible differences in the electronic properties of EHC materials must be reflected on the electron transfer kinetics associated with peak B/B´, an effective comparison of the electron transfer kinetics assessed by the peak to peak separation must be done with caution when the electrode materials present a porous layer. Accordingly, several authors have shown that porosity effects can lead to a decrease in the peak-to-peak separation, misleading what the real electrode material kinetics is [30–32]. For EHC1 and 18a, it was found a peak-to-peak separation of 70 and 76 mV, consistent with an apparent heterogeneous rate constant (K^0_{app}) of $2.27x10^{-2}$ cm s^{-1} and $1.37x10^{-2}$ cm s^{-1}, respectively, predicted by Nicholson equation [33]. These values are comparable to bare GCE

(K^0_{app} of $2.27x10^{-2}$ cm s^{-1}), which is indicative that the electronic properties of the high oxygen content of EHC materials and glassy carbon are very similar.

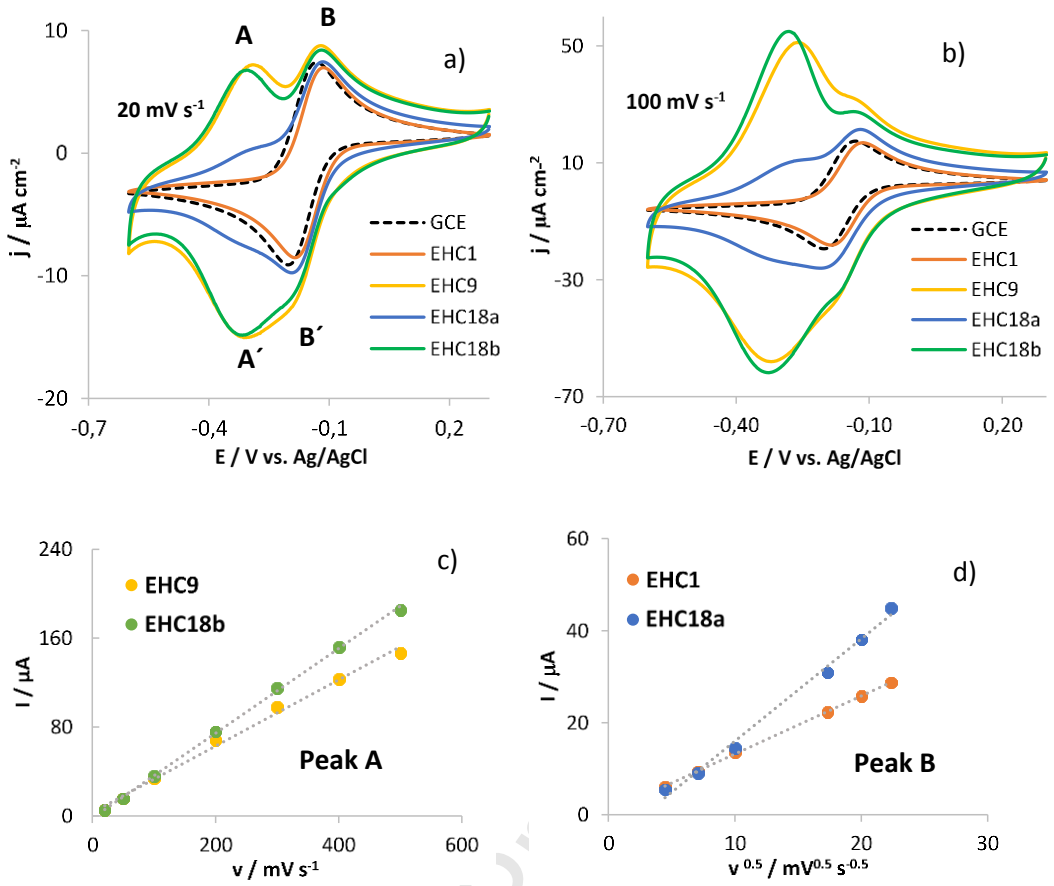

Fig. 5 - a) Cyclic voltammograms of glassy carbon and glassy carbon modified electrodes in 1 mM $Ru(NH_3)_6Cl_3$ + 0.1 M KCl solution at ν=20 mV s^{-1} and b) ν=100 mV s^{-1}. c) Corresponding plots of the current intensity peaks as a function of the scan rate (just for peak A), and d) as a function of the square root of the scan rate (just for peak B).

The electron transfer properties of the EHC electrodes were subsequently probed using another benchmark redox probe, $Fe(CN)_6^{3-/4}$. Ferrocyanide is known to be an inner-sphere redox probe, which means that it is not only sensitive to the electronic properties of the electrode material but is also highly sensitive to the surface chemistry, particularly to oxygen functional groups moieties.

In order to appraise possible carbon loadings effects, this study was undertaken with two different carbon loadings: 5 µg cm^{-2} (includes EHC1 and EHC18), and 20 µg cm^{-2} (comprises EHC9, 18a, and 18b). Fig. 6 shows the cyclic voltammetric response of EHC modified electrodes and bare GCE in a 0.1 M $Fe(CN)_6^{3-/4-}$ solution containing 0.1 M KCl background electrolyte. In this case, only one pair of peaks is present, pointing out that $Fe(CN)_6^{3-/4-}$ is not sensitive to the porosity of the electrode

surface. A possible reason for this behavior is probably the electrostatic repulsion by the negative surface charge of EHC materials, leading to the non-penetration of the electrolyte inside the EHC pores. Taking into account this assumption, the apparent heterogeneous electron-transfer rate constants, k^0_{app}, were calculated using the Nicholson equation. The results (Table 4) show that the heterogeneous electron transfer rates are of the same order of magnitude, but the electron kinetics of $Fe(CN)_6^{3-/4-}$ on EHC1 and EHC18a electrode is a little more sluggish than on GCE. Despite the O/C ratio on EHC1 is lower than on EHC18a, the heterogeneous electron transfer rate of EHC18a is higher and is not much affected by the electrode carbon loading (k^0_{app} of $1.73x10^{-3}$ and $1.95x10^{-3}$ cm/s for a loading of 5 and 20 µg/cm^2, respectively), reinforcing the conclusion that the electronic properties of EHC materials are not diminished by their oxygen-enriched composition.

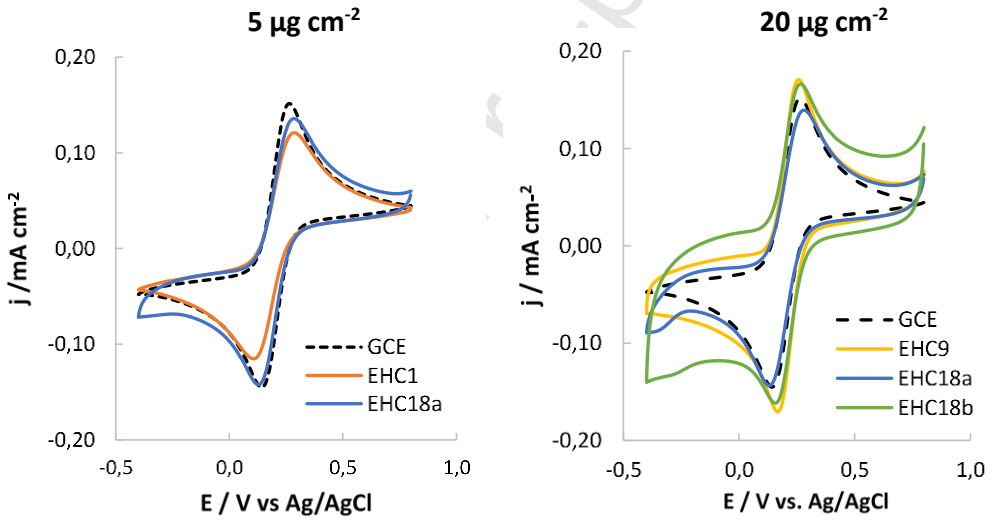

Fig. 6 - Cyclic voltammograms of glassy carbon and glassy carbon modified electrodes with different carbon loadings (5 µg cm^{-2} and 20 µg cm^{-2}) in 1 mM $Fe(CN)_6^{3-/4-}$ + 0.1 M KCl solution. ν=20 mV s^{-1}.

In order to obtain further insight into the electron-transfer properties, electrochemical impedance spectroscopy (EIS) was also carried out. Fig. 7a displays the Nyquist plots acquired for glassy carbon electrodes modified with two different loadings of EHC materials. The impedance spectra show a clear semicircle corresponding to charge transfer resistance (R_{ct}) in the high-frequency range for EHC1 and EHC18a materials, whereas a considerably smaller feature is shown for EHC9 and EHC18b.

The modified Randles circuit (Fig 7b) which was found to give the best fit to the experimental data (lowest $\chi 2$ value) presents the electrolyte resistance (R_s) in series with a parallel circuit composed of a constant phase element accounting for the double-layer (CPE_{dl}) and a charge transfer resistance (R_{ct}), itself in series with a constant phase element representing diffusion (CPE_W). It is noteworthy that despite a nearly 45^0 slope with respect to the real axis was clearly observed at the middle-low frequency region, data fitting considering a Warburg diffusion element yield very high χ^2 values, so a CPE was used with P values around 0.5, as discussed below. The fitting EIS data is given in Table 4.

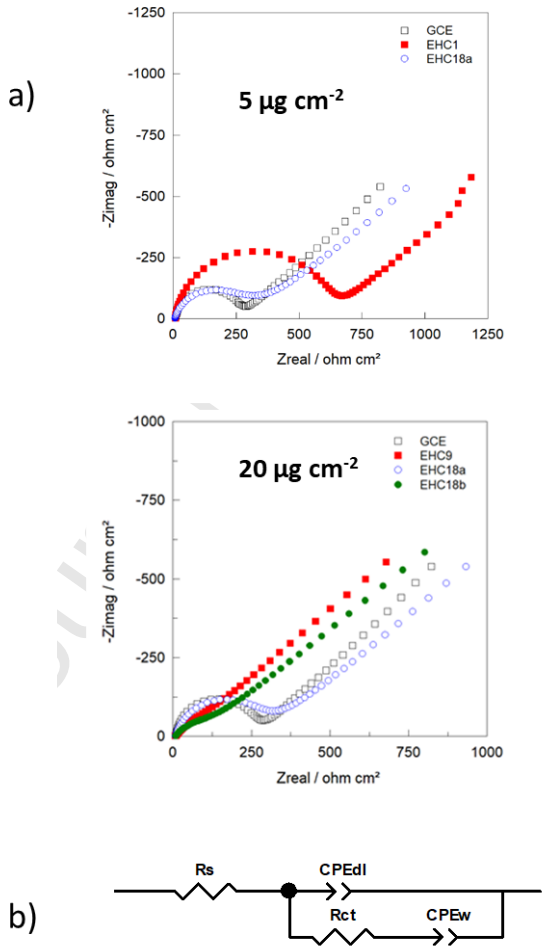

Fig. 7 – a) Nyquist plots from EIS for $Fe(CN)_6^{3-/4-}$ redox probe on glassy carbon and glassy carbon modified electrodes with different carbon loading: 5 µg cm^{-2} and 20 µg cm^{-2}. b) Modified Randles circuit to fit the experimental data.

Apart from EHC1, the resistance to electron transfer (R_{ct}) is about the same for all the EHC films (EHC9, 18a, and 18b), and not much different from GCE. Using the R_{ct} values obtained from the equivalent circuit fitting, the standard heterogeneous rate constant (k^0) was calculated from equation 4,

$$k^0 = \frac{R.T}{C_O^{\alpha} . C_R^{\alpha-1} . F^2 . R_{CT}} \quad (4)$$

where R is the gas constant, T the temperature, F the Faraday constant, c the bulk concentration for oxidized (O) and reduced species (R) and α the transfer coefficient (α=0.5). Electron transfer heterogeneous rates constants k^0 were found to range from 0.46 x 10^{-5} cm s^{-1} (EHC1) to 2.46x10^{-5} cm s^{-1} (EHC9). EIS-determined k^0 follows the same trend for k^0 obtained by CV, but a discrepancy of 2 orders of magnitude is found. A possible explanation for this disagreement relies on the overestimation of R_{ct}, caused by the surface passivation developed along with the timeframe of EIS, which is much longer than on voltammetry. Passivation of the surface electrode may result from the adsorption of ferrocyanide and ferricyanide ions or to the adsorption of Prussian Blue-like products, hindering the electrochemical reaction and consequently decreasing the electron transfer rate constant [34–36].

Material	Cyclic Voltammetry			EIS							
	Carbon loading (µg/cm^2)	ΔEp (mV)	K_{app} (10^{-3} cm/s)	R_s (Ω cm^2)	R_{ct} (Ω cm^2)	CPE_{dl}		CPE_{diff}		X^2	K_{app} (10^{-5} cm/s)
						CPE-T (µF cm^{-2} s^{1-P})	**CPE-P**	**CPE-T** (F cm^{-2} s^{1-P})	**CPE-P**		
GCE	0	122	2.99	10.13	250.3	13	0.938	4.60E-3	0.470	3.4E-04	1.11
EHC1	5	180	1.4	9.44	601.1	12	0.926	3.99E-3	0.458	1.2E-04	0.46
EHC18a		160	1.73	7.63	267.2	45	0.846	3.68E-3	0.409	1.7E-04	1.04
EHC9	20	92	6.32	8.93	112.8	398	0.652	3.48E-3	0.431	6.9E-05	2.46
EHC18a		150	1.95	7.96	282.9	44	0.822	4.03E-3	0.443	8.8E-05	0.98
EHC18b		110	3.82	8.82	148.6	1450	0.643	3.65E-3	0.452	5.4E-05	1.87

Table 4. Summary of cyclic voltammetric, EIS parameters data and corresponding apparent electron transfer rate constant (k_{app}) for GC and GC modified electrodes in 1 mM $Fe(CN)_6^{3-/4-}$ + 0.1 M KCl solution.

The impedance associated with CPE, regardless it is CPE_{dl} or CPE_W, is composed of two parameters, CPE-T and CPE-P, being defined as $Z = 1/[T(j\omega)^P]$. The CPE element only describes an ideal capacitor when CPE-P is 1. For GCE and EHC1 electrodes, the CPE_{dl}-P is close to one whereas for EHC9 and EHC18b it deviates considerably from the pure capacitor model. This behavior is suggestive of significant surface heterogeneity on these two electrode materials (coherent with their higher roughness/porosity). EHC18b also displays the highest CPE_{dl}-T value, indicative of a very high electrochemical surface area, in agreement with the high double-layer current exhibited in the cyclic voltammogram of Fig. 6. Note that for an accurate estimation of the electrochemical surface area one should employ an outer-sphere redox probe, like $Ru(NH_3)_6^{3+/2+}$, but due to the unexpected phenomenon described above, this calculation was not feasible.

Concerning the faradaic response and, in particular, the mass transfer effects, a CPE_W was used to fit the results. In fact, although a Warburg element would be the most appropriate choice for the electrical equivalent circuit, this element led to low-quality fitting with quite high χ^2 values. As the response of a pure Warburg element is equivalent to a constant phase element with P=0.5, this was the chosen element and, as depicted in Table 4, all the P values range from 0.4 to 0.5.

The overall EIS data reveals the intrinsic surface properties of EHC materials, reinforcing the results obtained by cyclic voltammetry. Accordingly, it is concluded that EHC9 material shows the fastest electron-transfer kinetics, followed by EHC18b, EHC18a, and EHC1. Despite the good ability of these materials for the electron transfer, determination of the conduction mechanism is a key missing piece that should be elucidated in the near future.

3.3 Electrocatalytic reduction of O_2

A comparison of the electrochemical behavior of EHC nanomaterials towards the ORR was firstly assessed by LSV in O_2-saturated 0.1M NaOH solution at zero rotation rate and 1600 rpm, Fig. 8a and 8b, respectively. For comparison purposes, Fig. 8a also presents the voltammetric curves obtained

with GCE and EHC nanomaterials in O_2-free solutions (dashed lines). Under no stirring conditions, the bare GCE exhibits two broad reduction peaks, one located at ca. 0.44 V and another at ca. 0.02 V. According to the literature, both peaks are ascribed to the reduction of O_2 to H_2O_2 (HO_2^- in 0.1 M NaOH). The first is assigned to the 2e-electrochemical reduction of O_2 mediated by active surface-oxygen groups (typically, quinone-like), while the second is attributed to the direct 2e-reduction reaction [37,38]. Alike the glassy carbon material, all EHC materials exhibit the first peak, but their intensity is significantly higher than on GCE, reflecting the higher amount of surface oxygen-containing groups that are able to mediate the reduction process (typically, the glassy carbon has an O/C ratio of 1-8 % [39]). Among EHC materials, EHC9 and EHC1 show respectively, the highest and the lowest reduction current intensity and the most and least positive potential onset, which are strong indicators of their relative catalytic activities for the ORR. Note also that the second reduction peak, at ≅ 0.02 V is not present on EHC1, contrasting with the other carbon materials.

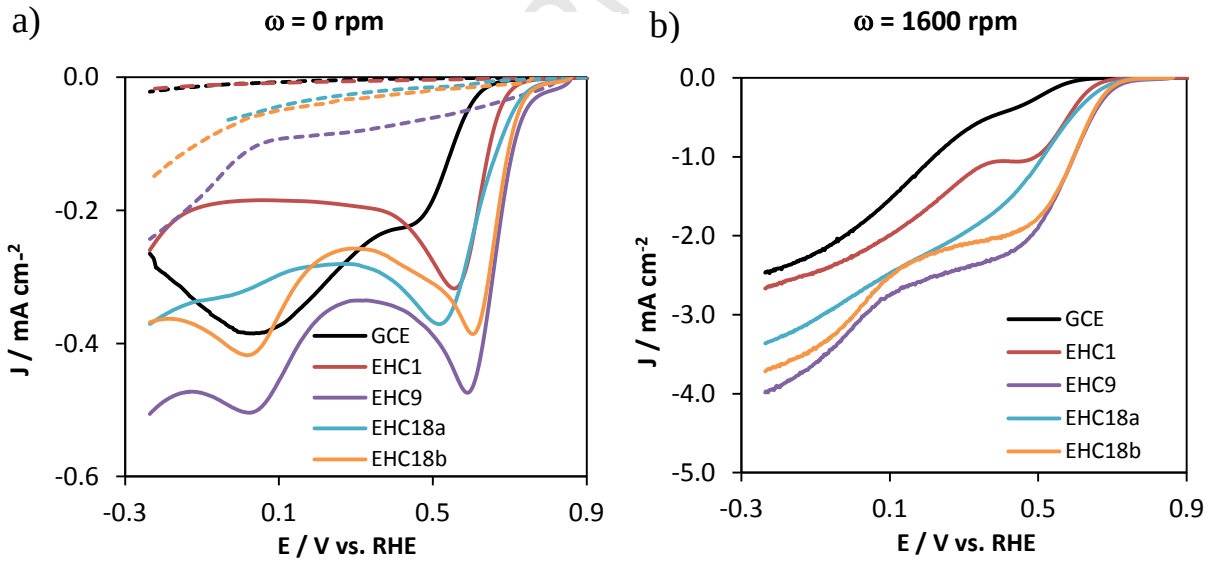

Fig.8- a) Linear voltammograms of glassy carbon and glassy carbon modified electrodes in O_2-saturated 0.1 M NaOH solution at 0 rpm and b) 1600 rpm. ν=20 mV s^{-1}.

Under stirring conditions (Fig. 8b), the potential onset follows the trend EHC9 ≅ EHC18b > EHC18a > EHC1 > GCE, Table 5. Despite the difficulty of extracting the half-wave potentials ($E_{1/2}$) from non-flat current plateaus, the obtained data provides a rough estimation of their comparative values, following also the trend depicted for the potential onset. The highest activity of EHC9 and EHC18b,

followed by EHC18a and EHC1, is also supported by a comparison of their kinetic current densities extracted at 0.67 V (vs RHE), a potential taken from the kinetically controlled potential region which satisfies the relation $0.1 < i/id < 0.5$ [40].

EHC	ω = 0 rpm		ω = 1600 rpm			
	Eonset (V)	j_p (mA/cm^2)	Eonset (V)	$E_{1/2}$ (V)	j_K (mA/cm^2) at 0.67 V	Tafel slope (mV/dec)
GCE	0.65	0.23	0.60	0.52	0.007	100
EHC1	0.73	0.32	0.67	0.57	0.07	83
EHC9	0.76	0.47	0.73	0.59	0.34	95
EHC18a	0.76	0.37	0.70	-----	0.16	96
EHC18b	0.76	0.39	0.73	0.59	0.30	74

Table 5. The ORR performance of glassy carbon and glassy carbon modified electrodes in O_2-saturated 0.1M NaOH solution under stirring and non-stirring conditions.

To further evaluate the ORR performance of the different EHC materials, RDE measurements were conducted at 400 to 2100 rpm rotation rates (Fig. S3) and the corresponding data was analyzed through the Koutecky-Levich (K-L) plots (j^{-1} vs. $\omega^{-1/2}$), Fig. 9a, to determine the number of electrons transferred per O_2 molecule (n_{O2}), Fig. 9b. It is shown that the number of electrons transferred on EHC1 and GCE is nearly 2.0 independently of the electrode potential, whereas the variation of *n* with potential on the other EHC materials is quite different. The highest number of electrons transferred (3.7-3.8) is exhibited by EHC9, pointing for its higher ability to convert O_2 to H_2O. The values of *n* on EHC18b and EHC18a are suggestive that these materials catalyze both the two-and four-electron pathways.

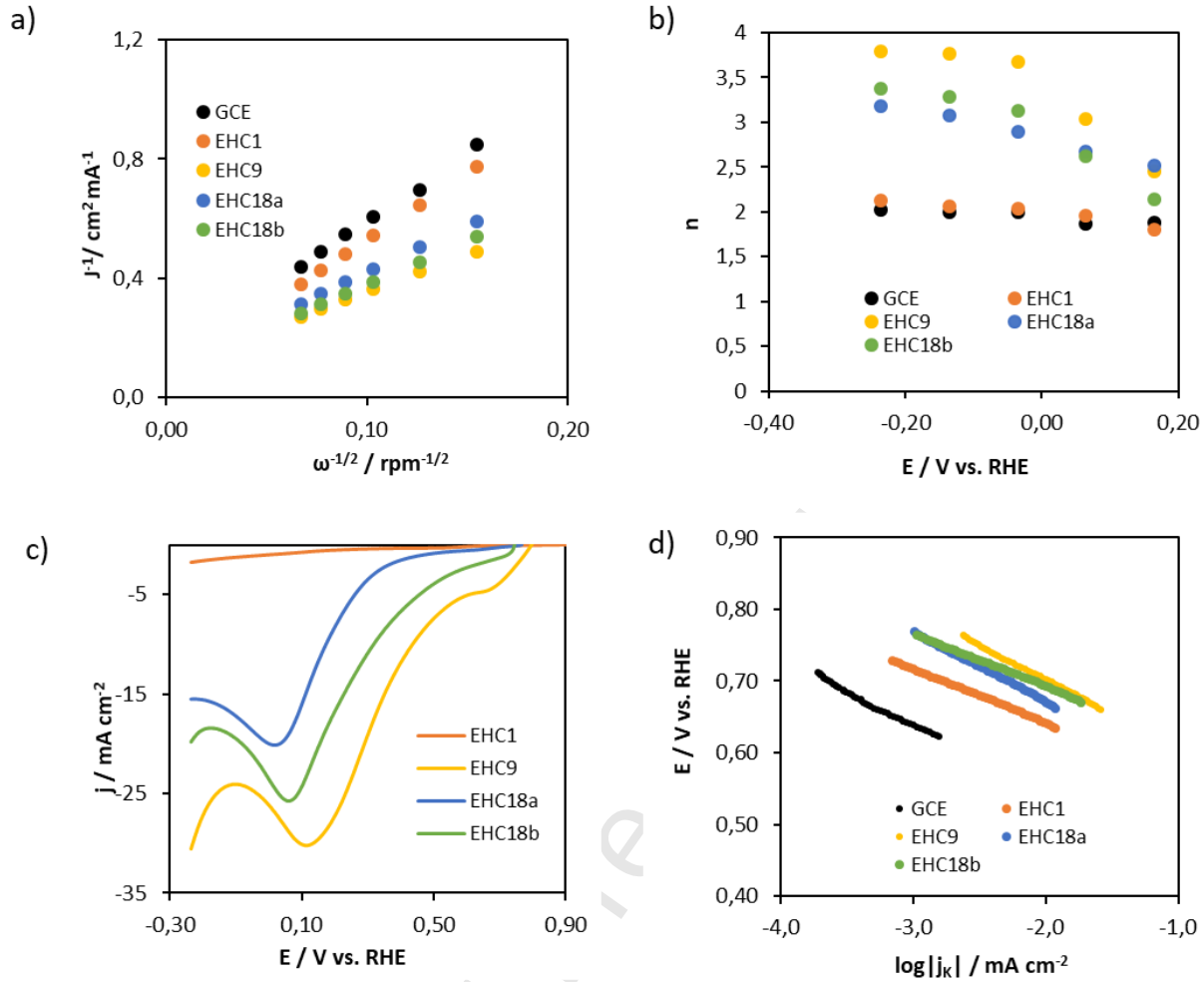

Fig.9- a) Koutecky-Levich plots at -0.04 V (vs RHE); b) Plot of the number of electrons transferred per O_2 molecule as a function of the electrode potential; c) LSV of glassy carbon modified electrodes in 0.85 µM H_2O_2 + 0.1 M NaOH solution at ν= 20 mV s^{-1}. Carbon loading: 1.3, 37.5, 13.3 and 12.4 µg cm^{-2} for EHC1, EHC9, EHC18a, and EHC 18b, respectively; d) Tafel plots for EHC nanomaterials and GCE.

For further insight on the ORR mechanism, the electrochemical reduction of hydrogen peroxide was conducted on the glassy carbon modified electrodes, Fig. 9c. The LSV curves for EHC9, EHC18a, and EHC18b show remarkably low potentials onset and high current density, compared to EHC1. The catalytic activity for the hydrogen peroxide reduction was found to follow the trend EHC9 > EHC18b > EHC18a >> EHC1, in agreement with the trend found for the ORR activity and the number of electrons involved in the O_2 electrochemical reduction reaction.

These results reinforce the conclusion that the ORR on EHC1 follows a 2e route and shows a negligible activity to reduce the hydrogen peroxide, whereas a 4e route occurs on the nanomaterials prepared by long-term electrode polarization (EHC9, 18a, and 18b). Actually, under the light of these

results, we would expect that hydrogen peroxide once formed would be promptly reduced on the EHC9, 18a and 18b in an O_2-saturated solution. The fact that the number of electrons on these electrode materials is rather low (*n*= 2-3) unless a negative potential is achieved (≅ - 0.03 V), may be explained by the blockage of surface sites required for the further reduction of peroxide. The formation of products or/and intermediate species that block the surface active sites along the O_2 reduction would also explain the unexpected high Tafel slope found on EHC9 and EHC18a (Table 5). Indeed, only EHC18b displays a low Tafel slope, approaching the 60 mV/dec value found on Pt [41].

In order to have the full picture of the electrocatalytic activity of EHC materials and the quantitative information regarding the oxygen functional groups (acquired by XPS), a 2D plot was constructed, in which the kinetic current at 0.67 V and the number of electrons at -0.04 V are the electrocatalytic descriptors, Figure 10. It is shown a direct correlation between the ***C***=O relative amount and the electroactivity, while the ***C***-O percentage *vs.* ORR descriptors shows a clear anticorrelation, that is, when ***C***-O is high, the electroactivity is low (for EHC1 and EHC18a) and when ***C***-O is relatively low, the electroactivity is high (for EHC9 and EHC18b).

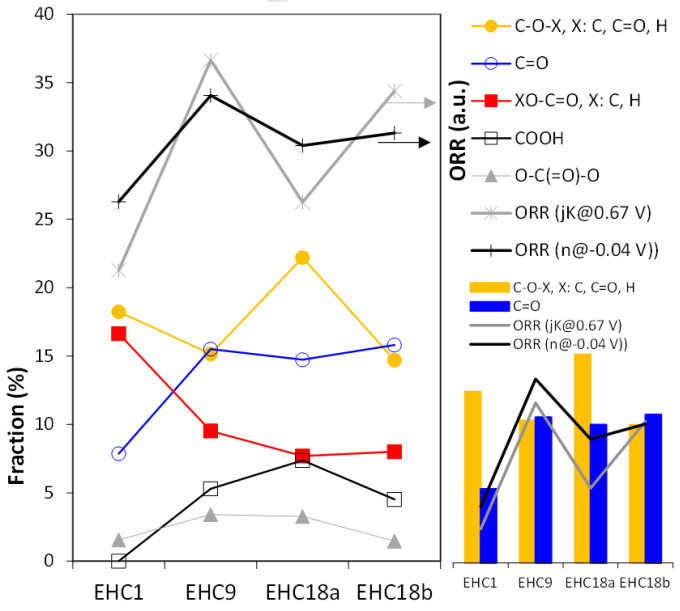

Fig. 10 - Fraction of oxidized carbon species and ORR descriptors for each sample. Carbon percentages are referred to as the left axis and ORR descriptors are referred to as the right axis. The inset shows how C-O (%) and C=O (%) compare with ORR descriptors where all the values are referred to the left axis except the ORR (n@-0.04 V) values which are referred to the right axis.

The overall results suggest that ***C***=O groups have an important role in the electrocatalysis, particularly in the O_2 and H_2O_2 reduction reactions. However, the differences found on the porosity of the electrode materials must also have an important impact on the apparent catalytic activity. Since it is impossible to separate these two effects, we advocate that the content of the ***C***=O functionality, together with the presence of a high surface porosity are responsible for the high activity displayed by EHC9 and EHC18b materials. These findings are in agreement with the argument that the carbonyl group facilitates the electron transfer on the oxygen reduction reaction [42,43].

4. Conclusions

In summary, it was demonstrated that the short and long-termed galvanostatic polarization of a graphite rod provides the anodic generation of carbon-based nanomaterials containing an anomalous high content of oxygen functionalities ($0.4 < O/C < 0.6$). The oxygen-containing groups are predominantly in the form of hydroxyl (or ether) and carboxyl on the short-termed electrogenerated materials, and in the form of hydroxyl and carbonyl (or epoxy) on those generated by a long-termed polarization. All these materials exhibit a very good electron-transfer ability (appraised by EIS and CV). It was found that the catalytic activity towards the oxygen reduction reaction was dictated by the content of the ***C***=O functionality, together with the high surface porosity. Although the best catalytic materials display a very high ability for the hydrogen peroxide reduction, a low conversion of O_2 to H_2O was found unless high overpotentials were achieved. These divergence results suggest the surface blockage by reaction intermediates in the early stages of the oxygen reduction reaction. Taken all together, this study provides a new perspective on the use of highly oxidized carbon nanomaterials in electrocatalysis.

Acknowledgments

This work was supported by Fundação para a Ciência e a Tecnologia (FCT), FEDER under program PT2020 through projects and project "UniRCell" with the reference POCI-01-0145-FEDER-016422. A. S. V. acknowledges FCT for projects PTDC/CTM-NAN/0994 and A. M. Ferraria acknowledges FCT for Grant SFRH/BPD/108338/2015. CQ-VR, CQB, *CQFM and IN and IBB,* I3N and CQE are financed by FCT through contract UID/QUI/00616/2019, UID/MULTI/00612/2013, UID/NAN/50024/2013 and UID/QUI/00100/2019, respectively. We also thank Prof. João Coutinho (UTAD) for the TOC analysis.

References

[1] M. Shao, Q. Chang, J. Dodelet, R. Chenitz, Recent Advances in Electrocatalysts for Oxygen Reduction Reaction, Chem. Rev. 116 (2016) 3594–3657. doi:10.1021/acs.chemrev.5b00462.

[2] A. Kulkarni, S. Siahrostami, A. Patel, J.K. Nørskov, Understanding Catalytic Activity Trends in the Oxygen Reduction Reaction, Chem. Rev. 118 (2018) 2302–2312. doi:10.1021/acs.chemrev.7b00488.

[3] D. Xiong, X. Li, L. Fan, Z. Bai, Three-Dimensional Heteroatom-Doped Nanocarbon for Metal-Free Oxygen Reduction Electrocatalysis: A Review, Catalysts. 8 (2018) 301. doi:10.3390/catal8080301.

[4] C. Li, H. Tan, J. Lin, X. Luo, S. Wang, J. You, Y.M. Kang, Y. Bando, Y. Yamauchi, J. Kim, Emerging Pt-based electrocatalysts with highly open nanoarchitectures for boosting oxygen reduction reaction, Nano Today. 21 (2018) 91–105. doi:10.1016/j.nantod.2018.06.005.

[5] E. Yeager, Electrocatalysts for O2 reduction, Electrochim. Acta. 29 (1984) 1527–1537. doi:10.1016/0013-4686(84)85006-9.

[6] M. Nunes, I. Rocha, D.M. Fernandes, A.S. Mestre, C. Moura, A.P. Carvalho, M.F. Pereira, C. Freire, Sucrose-derived activated carbons: electron transfer properties and application as oxygen reduction electrocatalysts, RSC Adv. 5 (2015) 102919–102931. doi:10.1039/C5RA20874B.

[7] C. Zhu, S. Dong, Recent progress in graphene-based nanomaterials as advanced electrocataysts toe«wards oxygen reduction reaction, Nanoscale. 5 (2013) 1753–1767. doi:10.1039/c2nr33839d.

[8] Y. Zheng, Y. Jiao, M. Jaroniec, Y. Jin, S.Z. Qiao, Nanostructured Metal-Free Electrochemical Catalysts for Highly Efficient Oxygen Reduction, Small. (2012) 3550–3566. doi:10.1002/smll.201200861.

[9] M. Inagaki, M. Toyoda, Y. Soneda, T. Morishita, Nitrogen-doped carbon materials, Carbon N. Y. 132 (2018) 104–140. doi:10.1016/j.carbon.2018.02.024.

[10] D. Wang, D. Su, Heterogeneous nanocarbon materials for oxygen, Energy Environ. Sci. (2014) 576–591. doi:10.1039/c3ee43463j.

[11] J. Zhu, S. Mu, Defect Engineering in the Carbon-Based Electrocatalysts: Insight into the Intrinsic Carbon Defects, Adv. Funct. Mater. 2001097 (2020) 1–19. doi:10.1002/adfm.202001097.

[12] Z. Qian, B. Sun, L. Du, S. Lou, C. Du, P. Zuo, Y. Ma, X. Cheng, Y. Gao, G. Yin, Insights into the role of oxygen functional groups and defects in the rechargeable nonaqueous Li e O 2 batteries, Electrochim. Acta. 292 (2018) 838–845. doi:10.1016/j.electacta.2018.09.202.

[13] L. Qin, W. Lv, W. Wei, F. Kang, D. Zhai, Q. Yang, Oxygen-enriched carbon nanotubes as a bifunctional catalyst promote the oxygen reduction / evolution reactions in Li-O 2 batteries, Carbon N. Y. 141 (2019) 561–567. doi:10.1016/j.carbon.2018.10.025.

[14] H. Zhang, K. Lv, B. Fang, M.C. Forster, R. Dervis, L.B. Andreas, K. Zhang, S. Chen, Crucial role for oxygen functional groups in the oxygen reduction reaction electrocatalytic activity of nitrogen-doped carbons, Electochimica Acta. 292 (2018) 942–950. doi:10.1016/j.electacta.2018.09.175.

[15] S. Wang, S. Dong, J. Wang, L. Zhang, P. Han, C. Zhang, X. Wang, K. Zhang, Z. Lan, G. Cui, Oxygen-enriched carbon material for catalyzing oxygen reduction towards hybrid electrolyte Li-air battery, J. Mater. Chem. 22 (2012) 21051–21056. doi:10.1039/c2jm34119k.

[16] D. Deng, L. Yu, X. Pan, S. Wang, X. Chen, P. Hu, L. Sun, X. Bao, Size effect of graphene on electrocatalytic activation of oxygen, Chem. Commun. 47 (2011) 10016–10018. doi:10.1039/c1cc13033a.

[17] M.C. Oliveira, A.S. Viana, M. Botelho, A.M. Ferraria, P.B. Tavares, A.D. Veloso, R.A. Videira, Dual Behaviour of Amorphous Carbon Released Electrochemically from Graphite, ChemistrySelect. 1 (2016) 4126–4130. doi:10.1002/slct.201600965.

[18] A.D. Veloso, A.M. Botelho do Rego, A.M. Ferraria, L.F.V. Ferreira, D.P. Ferreira, P.B. Tavares, R. Videira, A.S. Viana, M.C. Oliveira, One-Step Cathodic and Anodic Synthesis of Hydrophilic Carbon Nanomaterials, ChemElectroChem. 4 (2017) 2693–2702. doi:10.1002/celc.201700386.

[19] A.D. Veloso, A.M. Ferraria, M. Botelho, P.B. Tavares, P. Valento, D.D. Pereira, P.B. Andrade, A.J. Fernandes, M.C. Oliveira, R.A. Videira, Hydrophilic Carbon Nanomaterials : Characterisation by Physical , Chemical , and Biological Assays, ChemMedchemhem. 14 (2019) 1–14. doi:10.1002/cmdc.201900003.

[20] R.S. Vieira, A.J.S. Fernandes, M.C. Oliveira, Electrochemical behaviour of electrogenerated hydrophilic carbon nanomaterials, Electrochim. Acta. 260 (2018) 338–347. doi:10.1016/j.electacta.2017.10.197.

[21] R.E. Davis, G.L. Horvath, The solubility and diffusion coefficient of oxygen in potasium hydroxide solutions, Electochimica Acta. 12 (1967) 287–297. doi:10.1016/0013-4686(67)80007-0.

[22] R. Zhou, Y. Zheng, M. Jaroniec, S.Z. Qiao, Determination of the Electron Transfer Number for the Oxygen Reduction Reaction: From Theory to Experiment, ACS Catal. 6 (2016) 4720–4728. doi:10.1021/acscatal.6b01581.

[23] S. Xu, Y. Kim, D. Higgins, M. Yusuf, T.F. Jaramillo, F.B. Prinz, Building upon the Koutecky-Levich Equation for Evaluation of Next-Generation Oxygen Reduction Reaction Catalysts, Electrochim. Acta. 255 (2017) 99–108. doi:10.1016/j.electacta.2017.09.145.

[24] H.M.I. Jaim, D.P. Cole, L.G. Salamanca-riba, Characterization of carbon nanostructures in Al and Ag covetic alloys, Carbon N. Y. 111 (2016) 309–321. doi:10.1016/j.carbon.2016.10.007.

[25] S.A. Chernyak, A.S. Ivanov, K.I. Maslakov, A. V Egorov, Z. Shen, S. Savilov, V. V Lunin, Oxidation, defunctionalization and catalyst life cycle of carbon nanotubes: a Raman spectroscopy view†, Phys. Chem. Chem. Phys. 19 (2017) 2276–2285. doi:10.1039/C6CP04657F.

[26] D. Beamson, G. & Briggs, High resolution XPS of organic polymers. The Scienta ESCA300 Database, John Wiley, 1992.

[27] S. Wang, S. Dong, J. Wang, L. Zhang, P. Han, C. Zhang, X. Wang, K. Zhang, G. Cui, Oxygen-enriched carbon material for catalyzing oxygen reduction towards hybrid electrolyte Li-air battery †, (2012) 21051–21056. doi:10.1039/c2jm34119k.

[28] G.P. Keeley, M.E.G. Lyons, The Effects of Thin Layer Diffusion at Glassy Carbon Electrodes Modified with Porous Films of Single-Walled Carbon Nanotubes, 4 (2009) 794–809.

[29] A.J. Bard, L.R. Faulkner, J. Wiley, Chapter 6, in: Wiley (Ed.), Electrochem. Methods, 2 nd, New York, 2001: pp. 226–260.

[30] D. Menshykau, R.G. Compton, The Influence of Electrode Porosity on Diffusional Cyclic Voltammetry, (2008). doi:10.1002/elan.200804334.

[31] C. Punckt, M.A. Pope, I.A. Aksay, On the Electrochemical Response of Porous Functionalized Graphene Electrodes, (2013). doi:10.1021/jp405142k.

[32] C. Punckt, M.A. Pope, J. Liu, Y. Lin, A. Aksay, Electrochemical Performance of Graphene as Effected by Electrode Porosity and Graphene Functionalization, (2010) 2834–2841. doi:10.1002/elan.201000367.

[33] R.S. Nicholson, Theory and Application of Cyclic Voltammetry from Measurement of Electrode Reaction Kinetics, Anal. Chem. 37 (1965) 1351–1355.

[34] R. Alkire, P. Barlett, J. Lipkowski, Eletrochemistry of carbon electrodes, (2015).

[35] C.M. Pharr, P.R. Griffiths, Infrared Spectroelectrochemical Analysis of Adsorbed Hexacyanoferrate Species Formed during Potential Cycling in the Ferrocyanide / Ferricyanide Redox Couple, Anal. Chem. 69 (1997) 4673–4679. doi:10.1021/ac961120l.

[36] J. López-palacios, A. Heras, Á. Colina, V. Ruiz, Bidimensional spectroelectrochemical study on electrogeneration of soluble Prussian Blue from hexacyanoferrate (II) solutions, Electrochim. Acta. 49 (2004) 1027–1033. doi:10.1016/j.electacta.2003.10.013.

[37] J. Wu, Y. Wang, D. Zhang, B. Hou, Studies on the electrochemical reduction of oxygen catalyzed by reduced graphene sheets in neutral media, J. Power Sources. 196 (2011) 1141–1144. doi:10.1016/j.jpowsour.2010.07.087.

[38] M. Zhang, Y. Yan, K. Gong, L. Mao, Z. Guo, Y. Chen, Electrostatic Layer-by-Layer Assembled Carbon Nanotube Multilayer Film and Its Electrocatalytic Activity for O 2 Reduction, (2004) 8781–8785.

[39] S. Ranganathan, T. Kuo, R.L. Mccreery, Facile Preparation of Active Glassy Carbon Electrodes with Activated Carbon and Organic Solvents, 71 (1999) 3574–3580.

[40] K. Shinozaki, J.W. Zack, R.M. Richards, B.S. Pivovar, S.S. Kocha, Oxygen Reduction Reaction Measurements on Platinum Electrocatalysts Utilizing Rotating Disk Electrode Technique, J. Electrochem. Soc. 162 (2015) F1144–F1158. doi:10.1149/2.1071509jes.

[41] S.L. Gojkovi, S.K. Zecevic, R.F. Savinell, 02 Reduction on an Ink-Type Rotating Disk Electrode Using Pt Supported on High-Area Carbons, 145 (1998).

[42] L.R. Radovic, A.J.A. Salgado-Casanova, Hydrogen transfer and quinone/hydroquinone transitions in graphene-based materials, Carbon N. Y. 126 (2018) 443–451. doi:10.1016/j.carbon.2017.10.024.

[43] L.R. Radovic, A.J.A. Salgado-Casanova, C. V. Mora-Vilches, On the active sites for the oxygen reduction reaction catalyzed by graphene-based materials, Carbon N. Y. 156 (2020) 389–398. doi:10.1016/j.carbon.2019.09.059.

Captions

Fig. 1. – 3D AFM images of the different EHC nanomaterials. The bottom right-hand figure includes the 2D AFM image and the height profile of a diluted sample (EHC18b).

Fig. 2 - Raman spectra of the EHC nanomaterials and the corresponding bands.

Fig. 3 - C 1s XPS regions. Dashed lines are the fitted peaks positions. For detailed assignment see text. The carbon atoms of interest for each BE are highlighted in **bold**, *italic* and underlined. C1s regions are shifted on y-axis for clarity sake.

Fig. 4 - Quantification of the oxygen-functionalities on the EHC samples prepared at a different time (EHC 1, EHC9, EHC18a) and at different applied current in the galvanostatic electrolysis (EHC18b).

Fig. 5 - a) Cyclic voltammograms of glassy carbon and glassy carbon modified electrodes in 1 mM $Ru(NH_3)_6Cl_3$ + 0.1 M KCl solution at ν=20 mV s^{-1} and b) ν=100 mV s^{-1}. c) Corresponding plots of the current intensity peaks as a function of the scan rate (just for peak A), and d) as a function of the square root of the scan rate (just for peak B).

Fig. 6 - Cyclic voltammograms of glassy carbon and glassy carbon modified electrodes with different carbon loadings (5 µg cm^{-2} and 20 µg cm^{-2}) in 1 mM $Fe(CN)_6^{3-/4-}$ + 0.1 M KCl solution. ν=20 mV s^{-1}.

Fig. 7 – a) Nyquist plots from EIS for $Fe(CN)_6^{3-/4-}$ redox probe on of glassy carbon and glassy carbon modified electrodes with different carbon loading: 5 µg cm^{-2} and 20 µg cm^{-2}. b) Modified Randles circuit to fit the experimental data.

Fig.8- a) Linear voltammograms of glassy carbon and glassy carbon modified electrodes in O_2-saturated 0.1 M NaOH solution at 0 rpm and b) 1600 rpm. ν=20 mV s^{-1}.

Fig.9- a) Koutecky-Levich plots at -0.04 V (vs RHE); b) Plot of the number of electrons transferred per O_2 molecule as a function of the electrode potential; c) LSV of glassy carbon modified electrodes in 0.85 µM H_2O_2 + 0.1 M NaOH solution at ν= 20 mV s^{-1}. Carbon loading: 1.3, 37.5, 13.3 and 12.4 µg cm^{-2} for EHC1, EHC9, EHC18a and EHC 18b, respectively; d) Tafel plots for EHC nanomaterials and GCE.

Fig. 10 - Fraction of oxidized carbon species and ORR descriptors for each sample. Carbon percentages are referred to as the left axis and ORR descriptors are referred to as the right axis. The inset shows how C-O (%) and C=O (%) compare with ORR descriptors where all the values are referred to the left axis except the ORR (n@-0.04 V) values which are referred to the right axis.

Table 1. Galvanostatic conditions for the electrochemical generation of EHC nanomaterials.

Table 2. Peaks position, intensity and FWHM of D-, G- and a-C bands, as well as the I_D/I_G and $I_{a\text{-}C}/I_G$ ratio.

Table 3. Carbonaceous species: fractions of C 1s fitted peaks (at% /(C_{TOTAL} at%) × 100) and assignments; Atomic ratios: O(C_{OX})/C computed from peaks fitted in C 1s assuming minimum and maximum O/C stoichiometries; O/C computed from O 1s and C 1s total areas.

Table 4. Summary of cyclic voltammetric, EIS parameters data and corresponding apparent electron transfer rate constant (k_{app}) for GC and GC modified electrodes in 1 mM $Fe(CN)_6^{3-/4-}$ + 0.1 M KCl solution.

Table 5. The ORR performance of glassy carbon and glassy carbon modified electrodes in O_2-saturated 0.1M NaOH solution under stirring and non-stirring conditions

CRediT author statement

S.G. Meirinho: Investigation, Formal analysis

A. M. Ferraria: Investigation, Formal analysis

A. M. Botelho do Rego: Investigation, Formal analysis

A. J. S. Fernandes: nvestigation, Formal analysis

A. S. Viana: Investigation, Formal analysis

J.C.S. Fernandes: Investigation, Formal analysis

M.C. Oliveira: Conceptualization, Supervision, Investigation, Writing- Reviewing and Editing,

Declaration of interests

☒ The authors declare that they have no known competing financial interests or personal relationships that could have appeared to influence the work reported in this paper.

☐The authors declare the following financial interests/personal relationships which may be considered as potential competing interests:

Graphical Abstract

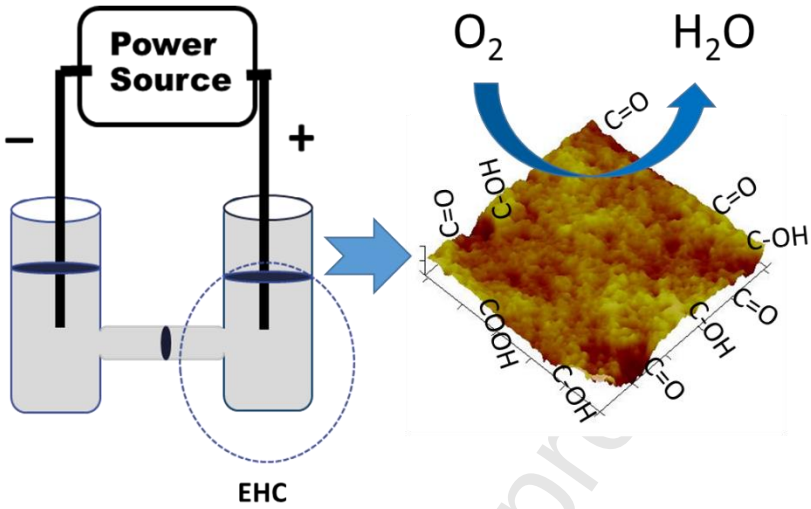

Highlights

- Approaches for the introduction of oxygen moieties on a carbon-based material.
- Surface characterization of oxygen-enriched nanomaterials (O/C $>$ 0.4).
- Electrode materials with a high electron-transport ability.
- Electrocatalytic activity towards oxygen and hydrogen peroxide reduction.